PAPER

Check for updates

Synthesis and biological evaluation of novel hybrid compounds bearing pyrazine and 1,2,4-triazole analogues as potent antitubercular agents†

Shivakumar Naik, [ID] [a] Dinesha Puttachari,[a] Vanishree A. L.,[a] Udayakumar D., [ID] *[a] Varsha Prakash Shetty,[b] Chaitra Prabhu[b] and Vijaya Kumar Deekshit[b]

In this study, we elucidate the conceptualization and synthesis of hybrid compounds (**T1–T18**) amalgamating pyrazine and 1,2,4-triazole scaffolds. A total of eighteen compounds were screened *in vitro* for their efficacy against the *Mycobacterium tuberculosis* H37Rv strain *via* the MABA assay. The results revealed that eight compounds (**T4**, **T5**, **T6**, **T11**, **T14**, **T15**, **T16**, and **T18**) manifested noteworthy activity against *Mtb*, with minimum inhibitory concentration (MIC) values of ≤21.25 μM. Furthermore, we also examined these compounds for their antibacterial and antifungal properties against various strains. Compounds **T4**, **T9**, **T10**, **T16**, and **T18** displayed significant antibacterial activity, while compounds **T12** and **T14** demonstrated significant antifungal activity. Subsequently, the most potent compounds were evaluated for their potential cytotoxicity to the Vero cell line *via* the MTT assay, revealing IC_{50} values surpassing 375 μM, indicative of minimal cytotoxicity. Additionally, we conducted *in silico* studies on these target molecules to better understand their action mechanisms. The *in silico* investigations suggest that the target enzyme involved in the action of the compounds may be DprE1. However, further experimental validation is necessary to ascertain the target responsible for the whole cell activity. All the target compounds are docked within the active site of the DprE1 enzyme, demonstrating favorable binding interactions. Furthermore, we predicted the ADME properties, physicochemical characteristics, and drug-like qualities of the target compounds using *in silico* methods. We also performed DFT studies to examine their electronic properties. These findings collectively indicate that the active compounds hold substantial promise as prospective contenders for the development of novel antitubercular agents.

Introduction

Tuberculosis (TB), an infectious disease caused by *Mycobacterium tuberculosis*, persists as a formidable global health challenge. With millions of new cases and deaths recorded annually, it endures as a predominant source of morbidity and mortality worldwide.[1] The advent of drug-resistant variants, notably multidrug-resistant tuberculosis (MDR-TB) and extensively drug-resistant tuberculosis (XDR-TB), has intensified the exigency for the formulation of groundbreaking and more efficacious antitubercular agents.[1] The current treatment regimens for TB are often lengthy, costly, and associated

with adverse side effects, underscoring the critical need for innovative therapies.[2] Over the preceding decades, notable advancements have transpired in the exploration of novel antimicrobial agents characterized by heightened efficacy and diminished toxicity. In this context, hybrid compounds have emerged as a compelling strategy to address the growing threat of drug-resistant TB.[3,4] Hybrid compounds are designed by combining distinct pharmacophores in a single molecule, leveraging the unique properties of each component to enhance biological activity. Pyrazine and 1,2,4-triazole analogues, well-known for their diverse pharmacological properties, have garnered substantial attention as potential building blocks for such hybrid compounds.[5,6]

Pyrazinamide serves as a primary pharmacotherapeutic agent in the treatment of tuberculosis, commonly employed in conjunction with other anti-TB medications. Its robust anti-TB efficacy plays a pivotal role in abbreviating the duration of tuberculosis therapy.[7] Various modified versions of pyrazinamide have been explored as effective antitubercular agents. For instance, Reddyrajula *et al.* investigated bioisosteric modifications of pyrazinamide derivatives, resulting in the develop-

[a]*Organic and Medicinal Chemistry Laboratory, Department of Chemistry, National Institute of Technology Karnataka, Surathkal-575025, Mangalore, Karnataka, India. E-mail: udayakumar@nitk.edu.in, udayaravi80@gmail.com*
[b]*Division of Infectious Diseases, NITTE University Center for Science Education and Research, NITTE (Deemed to be University), Deralakatte-575018, Mangalore, Karnataka, India*
†Electronic supplementary information (ESI) available. See DOI: https://doi.org/10.1039/d3pm00054k

ment of potent antitubercular compounds.[8] Srinivasarao and team have focused on *N*-(6-(4-(pyrazine-2-carbonyl)piperazine/homopiperazine-1-yl)pyridin-3-yl)benzamide derivatives as antitubercular agents.[9] Additionally, Panda *et al.* reported pyrazolopyridones as a novel class of noncovalent DprE1 inhibitors with strong anti-mycobacterial activity.[10] Zhou and his team have reported pyrazine-2-carboxamide derivatives that possess antitubercular properties.[11] Kumar *et al.* reported a series of pyrazine analogues as promising inhibitors of DprE1 for the treatment of tuberculosis.[12] In parallel, 1,2,4-triazoles, a subclass of five-membered heterocyclic compounds, have a well-established history of pharmacological importance. In recent research, Karczmarzyk and team have explored derivatives of 1,2,4-triazoles combined with pyridine for their antitubercular activity.[13] Oh *et al.* reported a series of 1,2,4-triazole derivatives with antitubercular properties.[14] Karabanovich *et al.* reported a series of 3,5-dinitrophenyl-containing 1,2,4-triazoles and their trifluoromethyl analogues as potent inhibitors of DprE1 for tuberculosis treatment.[15] Combining these two structural elements within a single hybrid molecule offers a unique opportunity to leverage their combined strengths, thereby potentially culminating in the conception of more potent and versatile antitubercular pharmaceutical agents. In light of the information provided, this study aims to illustrate the synthesis of an array of novel hybrid molecules by linking the pyrazine ring with a biologically active 1,2,4-triazole moiety to assess the effectiveness of these compounds in combating tuberculosis, evaluate their safety through cytotoxicity testing, investigate their physicochemical and pharmacokinetic properties, and explicate the plausible mechanism of action.

Materials and methods

The required chemical reagents were procured from diverse commercial suppliers, including Sigma Aldrich, TCI, and Alfa-Aesar. To monitor the progress of the chemical reaction, we employed TLC with alumina plates coated with silica gel (Merck 60 F254) as the stationary phase and a mobile phase comprising a 3:7 amalgamation of ethyl acetate and petroleum ether. Subsequently, we scrutinized the resultant spots under a UV chamber. For the determination of the melting points of the synthesized compounds, we utilized a digital melting point apparatus without any adjustments. Furthermore, for in-depth structural analysis, we conducted spectroscopic analysis on the synthesized compounds, encompassing proton nuclear magnetic resonance (1H-NMR) and carbon nuclear magnetic resonance (13C-NMR) spectroscopy. These spectroscopic assessments were carried out using a Bruker Avance Fourier transform-NMR (FT-NMR) spectrometer operating at 400 MHz for 1H-NMR and 100 MHz for 13C-NMR. CDCl₃ or DMSO-d6 was employed as a solvent, with tetramethyl silane (TMS) as an internal standard. Chemical shifts are articulated in parts per million on the δ-scale, while coupling constants are presented in Hertz (Hz). NMR spectral analysis was conducted utilizing Bruker NMR software (TopSpin

4.1.4). Furthermore, we acquired mass spectra of the synthesized compounds employing a Waters Xevo QTOF MS system equipped with an electrospray ionization (ESI) source.

Chemistry

Synthesis and characterization

Procedure for the synthesis of (Z)-pyrazine-2-carbohydrazonamide (2). In a clean and dry 100 mL round bottom flask, pyrazine-2-carbonitrile (1) (10 g, 95.14 mmol) was combined with anhydrous methanol (50 mL). To this mixture, hydrazine hydrate (8.33 mL, 166.50 mmol) was introduced. The reaction mixture was then stirred at room temperature for 24 hours. The progression of the reaction was scrutinized using thin-layer chromatography. Following the reaction, the obtained solid product was isolated by filtration, washed with cold methanol, and subsequently dried. The purification process involved recrystallization in methanol, resulting in the formation of yellow crystals.[16] Yield: 12.83 g, 98%; m.p.: 127–128 °C; 1H-NMR (CDCl₃, 400 MHz, δ in ppm): 9.24 (s, 1H), 8.48 (d, *J* = 2.36 Hz, 1H), 8.40 (d, *J* = 1.28 Hz, 1H), 5.10 (s, 2H), 4.70 (s, 2H); 13C-NMR (CDCl₃, 100 MHz, δ in ppm): 146.60, 146.44, 144.11, 142.81, 142.40; ESI-MS (*m/z*) = 106.03 [M + H]⁺.

Procedure for the synthesis of 5-(pyrazin-2-yl)-4H-1,2,4-triazole-3-thiol (3). Pyrazine-2-carbohydrazonide (2) (10 g, 72 mmol) and KOH (4.5 g, 80 mmol) were taken in anhydrous methanol (100 mL) in a clean 250 mL round bottom flask. Carbon disulfide (4.40 g, 72 mmol) was introduced into the reaction mixture and refluxed for 24 hours at 65 °C. The progress of the reaction was scrutinized using TLC. The reaction mixture was then cooled to room temperature and excess solvent was removed using a rotor-vap. The obtained residue was poured into crushed ice and made acidic (pH = 6) using 20% HCl, and the obtained solid was filtered and dried. Recrystallization was performed using methanol.[17] Pale yellow solid, yield: 92%, m.p.: 176–177 °C, 1H-NMR (DMSO-d6, 400 MHz, δ in ppm): 14.1692 (s, 1H), 13.9546 (s, 1H), 9.1809 (s, 1H), 8.7571 (s, 2H); 13C-NMR (DMSO-d6, 100 MHz, δ in ppm):167.9086, 148.3865, 145.8394, 144.3842, 142.3343, 140.5931, 40.1253, 39.9179, 39.7089, 39.5005, 39.2919, 39.0836, 38.8748; ESI-MS (*m/z*) = 180.03 [M + H]⁺.

General procedure for the synthesis of 1-phenyl-2-((5-(pyrazin-2-yl)-4H-1,2,4-triazol-3-yl)thio)ethan-1-one derivatives (T1–T9). A mixture of 5-(pyrazin-2-yl)-4H-1,2,4-triazole-3-thiol (3) (1.0 mmol) and sodium hydroxide (1.1 mmol) was taken in aqueous methanol (80%) (10 mL) in a clean 50 mL round bottom flask and the reaction mixture was stirred for 10 minutes at room temperature. Then substituted phenacyl bromide (1.0 mmol) was added and the reaction mixture was stirred at room temperature for 4 hours. The progression of the reaction was scrutinized using thin-layer chromatography. The reaction mixture was then poured into ice-cold water. The precipitated solid was filtered, washed with ice-cold water, and dried. Recrystallization was performed using methanol.[18]

1-Phenyl-2-((5-(pyrazin-2-yl)-4H-1,2,4-triazol-3-yl)thio)ethan-1-one (T1). White solid, yield: 86%; m.p.: 193–194 °C; 1H-NMR (CDCl₃, 400 MHz, δ in ppm): 12.7680 (s, 1H), 9.4716 (s, 1H), 8.6173 (s, 1H), 8.5612 (s, 1H), 8.0357 (s, 2H), 7.5983 (s, 1H),

7.4901 (d, J = 5.68 Hz, 2H), 5.0396 (s, 2H); ^{13}C-NMR (CDCl$_3$, 100 MHz, δ in ppm): 191.91, 166.40, 163.37, 146.63, 144.76, 144.07, 139.41, 134.92, 134.49, 129.15, 128.69, 41.97; ESI-MS (m/z) = 298.11 [M + H]$^+$.

2-((5-(Pyrazin-2-yl)-4H-1,2,4-triazol-3-yl)thio)-1-(p-tolyl)ethan-1-one (T2). White solid, yield: 88%; m.p.: 190–191 °C; ^{1}H-NMR (CDCl$_3$, 400 MHz, δ in ppm): 12.9680 (s, 1H), 9.4716 (s, 1H), 8.6260 (d, J = 2.16 Hz, 1H), 8.5711 (s, 1H), 7.9356 (d, J = 8.16 Hz, 2H), 7.2870 (d, J = 8.08 Hz, 2H), 5.0317 (s, 2H), 2.4134 (s, 3H); ^{13}C-NMR (CDCl$_3$, 100 MHz, δ in ppm): 191.53, 166.57, 163.36, 146.63, 145.66, 144.77, 144.09, 139.45, 132.45, 129.84, 128.83, 42.07, 21.99; ESI-MS (m/z) = 312.09 [M + H]$^+$.

1-(4-Methoxyphenyl)-2-((5-(pyrazin-2-yl)-4H-1,2,4-triazol-3-yl)thio)ethan-1-one (T3). White solid, yield: 93%; m.p.: 198–199 °C; ^{1}H-NMR (CDCl$_3$, 400 MHz, δ in ppm): 12.7783 (s, 1H), 9.4574 (s, 1H), 8.6143 (d, J = 2.44 Hz, 1H), 8.5622 (d, J = 1.44 Hz, 1H), 8.0076 (d, J = 8.8 Hz, 2H), 6.9419 (d, J = 8.84 Hz, 2H), 5.0007 (s, 2H), 3.8567 (s, 3H); ^{13}C-NMR (CDCl$_3$, 100 MHz, δ in ppm): 190.39, 166.70, 164.64, 163.35, 146.64, 144.79, 144.10, 139.47, 131.15, 127.95, 114.35, 55.81, 41.94; ESI-MS (m/z) = 328.13 [M + H]$^+$.

1-(4-Hydroxyphenyl)-2-((5-(pyrazin-2-yl)-4H-1,2,4-triazol-3-yl)thio)ethan-1-one (T4). White solid, yield: 87%; m.p.: 250–251 °C; ^{1}H-NMR (DMSO-d6, 400 MHz, δ in ppm): 12.9889 (s, 1H), 10.5739 (s, 1H), 9.3073 (s, 1H), 8.8451 (t, J = 5.80 Hz, 2H), 7.9481 (d, J = 8.52 Hz, 2H), 6.9016 (d, J = 8.52 Hz, 2H), 5.1359 (s, 2H); ^{13}C-NMR (DMSO-d6, 100 MHz, δ in ppm): 190.28, 165.39, 162.90, 162.87, 146.95, 145.02, 143.43, 138.69, 131.21, 126.43, 115.48; ESI-MS (m/z) = 314.06 [M + H]$^+$.

1-(4-Nitrophenyl)-2-((5-(pyrazin-2-yl)-4H-1,2,4-triazol-3-yl)thio)ethan-1-one (T5). White solid, yield: 81%; m.p.: 229–230 °C; ^{1}H-NMR (DMSO-d6, 400 MHz, δ in ppm): 12.6630 (s, 1H), 9.3847 (d, J = 1.20 Hz, 1H), 8.8110 (d, J = 2.48 Hz, 1H), 8.7697 (d, J = 1.52 Hz, 1H), 8.2163 (d, J = 8.68 Hz, 2H), 7.7926 (d, J = 8.64 Hz, 2H), 4.8030 (s, 2H); ^{13}C-NMR (DMSO-d6, 100 MHz, δ in ppm): 191.83, 164.80, 162.96, 150.21, 146.90, 144.92, 143.35, 139.54, 138.53, 129.85, 123.88; ESI-MS (m/z) = 343.08 [M + H]$^+$.

4-(2-((5-(Pyrazin-2-yl)-4H-1,2,4-triazol-3-yl)thio)acetyl)benzonitrile (T6). White solid, yield: 85%; m.p.: 215–216 °C; ^{1}H-NMR (DMSO-d6, 400 MHz, δ in ppm): 12.7140 (s, 1H), 9.3132 (d, J = 1.32 Hz, 1H), 8.8724 (d, J = 2.48 Hz, 1H), 8.8494 (t, J = 1.48 Hz, 1H), 8.4048 (d, J = 8.84 Hz, 2H), 8.3055 (d, J = 8.84 Hz, 2H), 5.2958 (s, 2H); ^{13}C-NMR (DMSO-d6, 100 MHz, δ in ppm): 190.28, 165.39, 162.90, 162.87, 146.95, 145.02, 143.43, 138.69, 131.21, 126.43, 121.44, 115.48; ESI-MS (m/z) = 323.10 [M + H]$^+$.

1-(4-Fluorophenyl)-2-((5-(pyrazin-2-yl)-4H-1,2,4-triazol-3-yl)thio)ethan-1-one (T7). White solid, yield: 92%; m.p.: 202–203 °C; ^{1}H-NMR (CDCl$_3$, 400 MHz, δ in ppm): 12.9680 (s, 1H), 9.4573 (s, 1H), 8.6234 (t, J = 1.56 Hz, 2H), 8.0875 (d, J = 5.56 Hz, 1H), 8.0679 (d, J = 5.56 Hz, 1H), 7.2400 (s, 1H), 7.1642 (t, J = 8.28 Hz, 1H), 5.0019 (s, 2H); ^{13}C-NMR (CDCl$_3$, 100 MHz, δ in ppm): 190.42, 167.87, 166.30, 165.32, 163.46, 146.70, 144.79, 144.11, 139.40, 131.57, 131.47, 116.56, 116.34, 41.69; ESI-MS (m/z) = 316.09 [M + H]$^+$.

1-(4-Chlorophenyl)-2-((5-(pyrazin-2-yl)-4H-1,2,4-triazol-3-yl)thio)ethan-1-one (T8). White solid, yield: 96%; m.p.: 197–198 °C; ^{1}H-NMR (DMSO-d6, 400 MHz, δ in ppm): 12.9686 (s, 1H), 9.4573 (s, 1H), 8.6234 (t, J = 1.56 Hz, 2H), 8.0875 (d, J = 5.56 Hz, 1H), 8.0679 (d, J = 5.56 Hz, 1H), 7.2400 (s, 1H), 7.1642 (t, J = 8.28 Hz, 1H), 5.0019 (s, 2H); ^{13}C-NMR (DMSO-d6, 100 MHz, δ in ppm): 190.84, 166.21, 163.48, 146.70, 144.79, 144.11, 141.14, 139.38, 130.11, 129.55, 41.64; ESI-MS (m/z) = 332.04 [M + H]$^+$.

1-(4-Bromophenyl)-2-((5-(pyrazin-2-yl)-4H-1,2,4-triazol-3-yl)thio)ethan-1-one (T9). White solid, yield: 94%; m.p.: 203–204 °C; ^{1}H-NMR (CDCl$_3$, 400 MHz, δ in ppm): 12.8630 (s, 1H), 9.4631 (s, 1H), 8.6313 (s, 1H), 8.5737 (s, 1H), 7.9071 (d, J = 7.00 Hz, 2H), 7.6406 (d, J = 7.08 Hz, 2H), 4.9843 (s, 2H); ^{13}C-NMR (CDCl$_3$, 100 MHz, δ in ppm): 191.07, 166.21, 163.50, 146.72, 144.80, 144.13, 139.40, 133.73, 132.57, 130.18, 129.97, 41.61; ESI-MS (m/z) = 375.99 [M + H]$^+$.

General procedure for the synthesis of 2-(5-(benzylthio)-4H-1,2,4-triazol-3-yl)pyrazine derivatives (T10–T18). A mixture of 5-(pyrazin-2-yl)-4H-1,2,4-triazole-3-thiol (**3**) (1.0 mmol) and potassium carbonate (1.0 mmol) was taken in acetone (10 mL) in a clean 50 mL round bottom flask and the reaction mixture was stirred for 10 minutes at room temperature. Then, substituted benzyl bromide (1.0 mmol) was introduced and the reaction mixture was stirred at room temperature for 2 hours. The progression of the reaction was scrutinized using thin-layer chromatography. The reaction mixture was then poured into ice-cold water. The precipitated solid was filtered, washed with ice-cold water, and dried. Recrystallization was performed using methanol.[18]

2-(5-(Benzylthio)-4H-1,2,4-triazol-3-yl)pyrazine (T10). Brown solid, yield: 96%; m.p.: 198–199 °C; ^{1}H-NMR (CDCl$_3$, 400 MHz, δ in ppm): 12.7482 (s, 1H), 9.5144 (d, J = 1.00 Hz, 1H), 8.6320 (d, J = 2.44 Hz, 1H), 8.5723 (d, J = 1.44 Hz, 1H), 7.4541 (d, J = 7.16 Hz, 2H), 7.3169 (m, J = 6.88 Hz, 3H), 4.6244 (s, 2H); ^{13}C-NMR (CDCl$_3$, 100 MHz, δ in ppm): 168.19, 162.49, 160.02, 145.89, 144.90, 144.38, 142.46, 131.67, 131.63, 130.20, 130.11, 124.49, 31.46; ESI-MS (m/z) = 270.08 [M + H]$^+$.

2-(5-((4-(Trifluoromethyl)benzyl)thio)-4H-1,2,4-triazol-3-yl)pyrazine (T11). White solid, yield: 92%; m.p.: 154–155 °C; ^{1}H-NMR (DMSO-d6, 400 MHz, δ in ppm): 12.9783 (s, 1H), 9.3917 (d, J = 1.36 Hz, 1H), 8.8125 (d, J = 2.56 Hz, 1H), 8.7720 (t, J = 1.52 Hz, 1H), 7.7360 (s, 2H), 7.6738 (s, 2H), 4.7617 (s, 2H); ^{13}C-NMR (DMSO-d6, 100 MHz, δ in ppm): 168.19, 162.49, 160.02, 145.89, 144.90, 144.36, 142.46, 131.66, 131.63, 130.20, 130.11, 115.63; ESI-MS (m/z) = 338.11 [M + H]$^+$.

2-(5-((4-Fluorobenzyl)thio)-4H-1,2,4-triazol-3-yl)pyrazine (T12). White solid, yield: 86%; m.p.: 150–151 °C; ^{1}H-NMR (CDCl$_3$, 400 MHz, δ in ppm): 12.8980 (s, 1H), 9.4857 (d, J = 1.12 Hz, 1H), 8.6161 (d, J = 2.44 Hz, 1H), 8.5516 (t, J = 1.52 Hz, 1H), 7.4241 (d, J = 5.40 Hz, 1H), 7.4030 (d, J = 5.36 Hz, 1H), 7.0115 (s, 1H), 6.9791 (d, J = 8.60 Hz, 1H), 4.5731 (s, 2H); ^{13}C-NMR (CDCl$_3$, 100 MHz, δ in ppm): 167.88, 163.78, 161.34, 145.90, 144.85, 144.37, 142.45, 131.74, 131.71, 131.17, 131.09, 115.78, 37.44; ESI-MS (m/z) = 288.08 [M + H]$^+$.

2-(5-((2-Fluorobenzyl)thio)-4H-1,2,4-triazol-3-yl)pyrazinepyrazine (T13). Yellow solid, yield: 98%; m.p.: 130–131 °C; ^{1}H-NMR (CDCl$_3$, 400 MHz, δ in ppm): 12.9637 (s, 1H), 9.5007 (d, 1H),

8.6205 (d, J = 2.52 Hz, 1H), 8.5582 (t, J = 1.56 Hz, 1H), 7.5256 (m, J = 1.56 Hz, 1H), 7.2660 (m, J = 2.04 Hz, 1H), 7.0876 (m, J = 7.60 Hz, 2H), 4.6542 (s, 2H); ^{13}C-NMR (CDCl$_3$, 100 MHz, δ in ppm): 168.19, 162.49, 160.02, 145.89, 144.90, 144.38, 142.46, 131.67, 131.63, 130.20, 130.11, 115.73, 31.46; ESI-MS (m/z) = 288.10 [M + H]$^+$.

4-(((5-(Pyrazin-2-yl)-4H-1,2,4-triazol-3-yl)thio)methyl)benzonitrile (T14). White solid, yield: 89%; m.p.: 209–210 °C; ^{1}H-NMR (DMSO-d6, 400 MHz, δ in ppm): 12.9220 (s, 1H), 9.3871 (d, 1H), 8.8122 (d, J = 2.52 Hz, 1H), 8.7701 (t, J = 1.56 Hz, 1H), 7.8314 (d, J = 8.28 Hz, 2H), 7.7139 (d, J = 8.24 Hz, 2H), 4.7464 (s, 2H); ^{13}C-NMR (DMSO-d6, 100 MHz, δ in ppm): 167.39, 163.89, 159.34, 146.58, 144.95, 142.62, 141.39, 132.49, 130.13, 123.49, 120.13, 110.37; ESI-MS (m/z) = 295.07 [M + H]$^+$.

2-(5-((4-Bromobenzyl)thio)-4H-1,2,4-triazol-3-yl)pyrazine (T15). Brown solid, yield: 92%; m.p.: 155–156 °C; ^{1}H-NMR (DMSO-d6, 400 MHz, δ in ppm): 12.9880 (s, 1H), 8.8150 (d, J = 2.52 Hz, 1H), 8.7779 (d, J = 1.52 Hz, 1H), 7.5579 (d, J = 8.40 Hz, 2H), 7.4731 (d, J = 8.44 Hz, 2H), 4.6444 (s, 2H); ^{13}C-NMR (DMSO-d6, 100 MHz, δ in ppm): 168.09, 163.79, 161.34, 146.54, 144.93, 143.72, 141.37, 135.99, 131.50, 131.35, 120.89; ESI-MS (m/z) = 347.98 [M + H]$^+$.

2-(5-((2-Bromobenzyl)thio)-4H-1,2,4-triazol-3-yl)pyrazine (T16). Brown solid, yield: 92%; m.p.: 156–157 °C; ^{1}H-NMR (CDCl$_3$, 400 MHz, δ in ppm): 12.9889 (s, 1H), 9.5008 (d, J = 1.28 Hz, 1H), 8.6200 (d, J = 2.48 Hz, 1H), 8.5581 (t, J = 1.56 Hz, 1H), 7.6238 (m, J = 6.08 Hz, 1H), 7.5658 (m, J = 7.04 Hz, 1H), 7.2533 (m, J = 6.44 Hz, 1H), 7.1454 (m, J = 6.12 Hz, 1H), 4.7505 (s, 2H); ^{13}C-NMR (CDCl$_3$, 100 MHz, δ in ppm): 168.19, 162.49, 160.02, 145.89, 144.90, 144.38, 142.46, 131.67, 131.63, 130.20, 130.11, 115.94, 31.46; ESI-MS (m/z) = 347.97 [M + H]$^+$.

2-(5-((4-Chlorobenzyl)thio)-4H-1,2,4-triazol-3-yl)pyrazine (T17). White solid, yield: 94%; m.p.: 162–163 °C; ^{1}H-NMR (CDCl$_3$, 400 MHz, δ in ppm): 12.9881 (s, 1H), 9.4932 (d, J = 1.20 Hz, 1H), 8.6239 (d, J = 2.48 Hz, 1H), 8.5600 (t, J = 1.60 Hz, 1H), 7.3880 (d, J = 8.40 Hz, 2H), 7.2692 (t, J = 8.40 Hz, 2H), 4.5689 (s, 2H); ^{13}C-NMR (CDCl$_3$, 100 MHz, δ in ppm): 168.09, 163.79, 161.34, 145.90, 144.85, 144.37, 142.45, 131.74, 131.71, 131.17, 131.09, 116.00, 37.44; ESI-MS (m/z) = 304.05 [M + H]$^+$.

2-(5-((4-Nitrobenzyl)thio)-4H-1,2,4-triazol-3-yl)pyrazine (T18). White solid, yield: 97%; m.p.: 194–195 °C; ^{1}H-NMR (DMSO-d6, 400 MHz, δ in ppm): 12.9680 (s, 1H), 9.3846 (d, J = 1.16 Hz, 1H), 8.8109 (d, J = 2.52 Hz, 1H), 8.7696 (d, J = 1.48 Hz, 1H), 8.2163 (d, J = 8.68 Hz, 2H), 7.7925 (d, J = 8.68 Hz, 2H), 4.8030 (s, 2H); ^{13}C-NMR (DMSO-d6, 100 MHz, δ in ppm): 167.83, 167.34, 146.85, 146.57, 144.93, 144.78, 143.67, 141.37, 130.40, 123.67; ESI-MS (m/z) = 315.08 [M + H]$^+$.

Computational studies

Pharmacokinetic and physicochemical studies. The complex processes governing how a pharmaceutical agent moves within the body are summarized by the acronym ADME, representing absorption, distribution, metabolism, and excretion. A deep understanding of these ADME intricacies is essential when developing pharmaceutical substances that achieve a balanced combination of safety and effectiveness.[19] In our efforts to predict the pharmacokinetic properties of the target compounds, we have utilized the computational capabilities of Schrödinger's qikprop program.[20]

In silico molecular docking studies. In this investigation, we utilized computational techniques to scrutinize how the ligand molecules interact with a target receptor. To do this, we employed a software, AutoDock-Vina 1.1.2.[21,22] First, we created the chemical structures of the ligand molecules we wanted to study using ChemDraw Professional 20.1.1 software. Then, we optimized their 3D structures using Chem3D 20.1.1 software.[23] The receptor's crystal structure was obtained from the Protein Data Bank (PDB ID: 4P8N). However, this structure had some missing components, including residues and atoms, which we needed to rectify. We accomplished this by using the Modeller tool to complete and refine the receptor's structure.[24] Before we proceeded with the actual docking simulation, we prepared the receptor by removing all non-protein elements, such as cofactors, ligands already attached to the receptor, water molecules, and heteroatoms. Additionally, we added polar hydrogens and applied Kollman charges to ensure an accurate representation of the receptor's electrostatic properties. To identify the exact location of the receptor's active site, we made use of the online COACH server.[25] Understanding the active site is critical because it's where the ligands will bind and interact with the receptor. We then set up the docking simulation by defining a specific area around the protein where we wanted to explore binding interactions. This area was represented by a cubical grid with dimensions of 100 × 100 × 105, possessing intervals of −0.389 Å, −3.917 Å, and 4.861 Å along the x, y, and z axes, respectively. Finally, we conducted docking using the Vina software, with an exhaustiveness parameter set to 16, which controls the thoroughness of the search for optimal binding positions between the receptor and the target molecules.

DFT studies. The molecular structures of the title compounds were optimized employing density functional theory (DFT) coupled with a 6-31G++ (d, p) basis set, incorporating Beck's three-parameter exchange function and the Lee–Yang–Parr nonlocal correlation functional, denoted as B3LYP.[26] The computational computations were executed utilizing the Schrödinger materials science package.[20] To enhance comprehension of the charge transfer phenomena and the disparities in energy among molecular orbitals, a meticulous analysis known as Frontier molecular orbital (FMO) evaluation was conducted. This analytical methodology facilitated the determination of the energy levels of the highest occupied molecular orbital (HOMO) and the lowest unoccupied molecular orbital (LUMO). After these energy differentials, we extracted indispensable chemical reactivity parameters providing insightful perspectives into the stability and reactivity attributes of the synthesized compounds.

Biological studies

In vitro antitubercular activity. The evaluation of the efficacy of the title compounds against *M. tuberculosis* entailed employing the microplate Alamar blue assay (MABA) technique. This

methodology, characterized by its gentleness, leverages the utilization of a robust, cell-permeable substance denominated resazurin.[27] To obviate desiccation of the culture medium during the incubation phase, 200 μL of sterile deionized water was instilled into all wells of sterile 96-well plates. The compounds of interest, alongside standard pharmaceutical agents, were meticulously prepared in two-fold dilutions (50.0, 25.0, 12.5, 6.25, 3.12, 1.56, and 0.78 μg mL^{-1}) through dissolution in dimethyl sulfoxide (DMSO). After this, 100 μL of Middlebrook 7H9 broth, augmented with 0.2% glycerol and 10% oleate-albumin dextrose-catalase (OADC), were introduced into the wells. Concurrently, 100 μL of *M. tuberculosis* H37Rv (ATCC27294) were inoculated into the 7H9 broth wells containing ten-fold serial dilutions of the pharmaceutical agents per milliliter. The plates were hermetically sealed with parafilm and incubated at 37 °C for five days. Post this incubation period, a freshly concocted amalgamation of Alamar blue reagent and a 10% solution of Tween 80 in a 1 : 1 ratio was added to the wells. A subsequent 24-hour incubation at 37 °C ensued. Thereafter, a visual examination of the well contents was carried out, with a pink hue signifying bacterial proliferation and a blue tint indicating the suppression of bacterial growth. The minimum inhibitory concentration was delineated as the lowest concentration of a compound required to impede bacterial growth. For comparative analysis, pyrazinamide (PZA), ciprofloxacin (INN), and streptomycin (STM) were employed as benchmark pharmaceuticals.

In vitro antibacterial and antifungal activity (broth microdilution method)

Bacterial isolates. Overnight-cultured pure strains of two Gram-positive bacteria (*Staphylococcus aureus*, *Streptococcus mutans*) and two Gram-negative bacteria (*Escherichia coli*, *Salmonella Typhi*) were introduced into Mueller Hinton Broth (MHB) and permitted to proliferate at 37 °C until reaching a density akin to 0.5 McFarland unit. A 96-well microtiter plate was employed, with 95 μl of MHB added uniformly across all wells. Initially, 100 μl of the compound was introduced into the initial well and thoroughly amalgamated through pipetting. Sequentially, 100 μl from the initial well was transposed to the subsequent well, and this process continued up to the ninth well, while the suspension from the ninth well was discarded. Subsequently, 5 μl of the respective bacterial cultures was added to all wells. The tenth well functioned as a compound control, containing 95 μl of MHB and 100 μl of the compound. The eleventh, well-acted as a culture control, harboring 95 μl of MHB and 5 μl of the bacterial culture. Finally, the twelfth well operated as a media control, containing solely 95 μl of MHB.

Fungal isolates. The pure fungal culture of *Aspergillus niger*, cultivated overnight, was strategically applied in small doses onto potato dextrose agar (PDA) plates. These plates were subjected to an incubation period at 30 °C lasting 3 to 4 days, fostering the proliferation of an extensive layer of fungal spores. Subsequently, these spores were meticulously harvested using sterilized cotton swabs and then suspended in potato dextrose broth (PDB). A 96-well microtiter plate was meticulously prepared, with each well receiving 95 μl of Mueller–Hinton Broth (MHB). Initially, 100 μl of a particular compound was added to the first well, thoroughly blending it using precise pipetting techniques. This process of transferring 100 μl from each well to the subsequent one was rigorously executed until reaching the ninth well, after which the resultant suspension was carefully discarded. At this stage, 5 μl of the previously prepared fungal spore suspension was uniformly introduced into all wells, except for the tenth well, designated as the compound control, containing 95 μl of MHB and 100 μl of the compound. The eleventh well served as a control for the culture, comprising 95 μl of MHB and 5 μl of fungal spores. Finally, the twelfth well functioned as the media control, solely containing 95 μl of MHB without any additional components.

Cytotoxicity studies

The Vero cell line, sourced from the National Center for Cell Sciences (NCCS) in Pune, India, comprises African green monkey kidney cells designated by Catalog number 11965-092. These cellular entities were cultivated in 96-well flat-bottomed microtiter plates utilizing DMEM supplemented with 10% heat-inactivated fetal calf serum (FBS) and 1% antibiotic–antimycotic 100× solution.[28] Subsequently, they were housed in an incubator maintained at a temperature of 37 °C, 95% humidity, and 5% CO$_2$ concentration for 24 hours. The cellular entities were then exposed to these distinct drug concentrations and subjected to an additional incubation period of 72 hours. Following this incubation, a thorough washing of cells in each well was executed using a phosphate buffer solution. After this step, a meticulously prepared stock solution of MTT (20 μL, 5 mg mL^{-1} in sterile phosphate-buffered saline) was instilled into each well, followed by an additional incubation for 4 hours in an environment comprising 5% CO$_2$. Upon removal of the supernatant, 100 μL of DMSO was introduced to dissolve the precipitated crystals. The absorbance levels of the wells housing the cells and the corresponding blanks were quantified at 570 nm using a microplate reader. The determination of the extent of growth inhibition was executed through the application of the following formula: % Growth Inhibition = (mean optical density (OD) of the test compound/mean OD of the negative control) × 100.

Results and discussion

Chemistry

Based on the favorable results obtained through *in silico* studies, we have progressed toward the synthesis of the envisioned compounds by following the synthetic pathways outlined in Scheme 1. The process commenced with the reaction of readily available pyrazine-2-carbonitrile (**1**) with hydrazine hydrate in the presence of methanol, yielding (*Z*)-pyrazine-2-carbohydrazonamide (**2**). Subsequently, compound **2** underwent cyclization when treated with KOH and CS$_2$, resulting in the formation of 5-(pyrazin-2-yl)-4*H*-1,2,4-triazole-3-thiol (**3**).
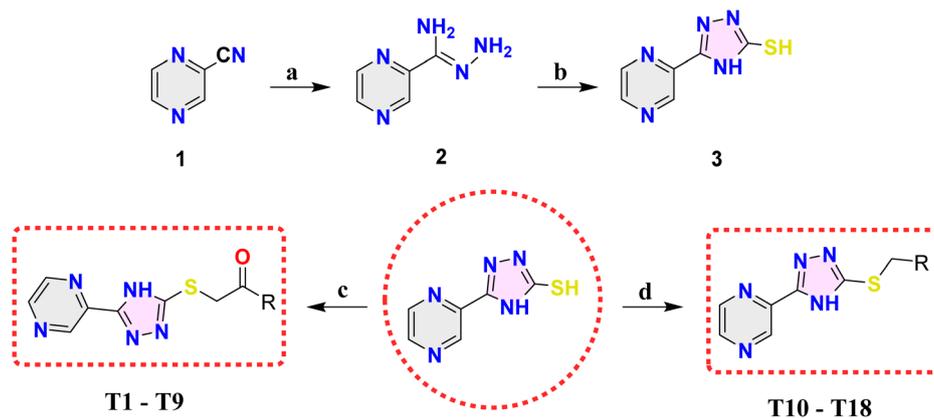
Scheme 1 Synthesis protocol for the synthesis of target compounds **T1–T18**. Reagents and conditions: (a) $N_2H_4 \cdot H_2O$, CH_3OH, RT, 24 hours, (b) CS_2, KOH, CH_3OH, reflux, 24 hours, (c) phenacyl bromide derivatives, 10% NaOH, CH_3OH, RT, 6 hours and (d) benzyl bromide derivatives, K_2CO_3, acetone, reflux, 2 hours.

Compounds **T1–T9** (Table 1) were produced by reacting compound **3** with commercially accessible phenacyl bromides, while compounds **T10–T18** (Table 1) were synthesized by reacting compound **3** with commercially available substituted benzyl bromides.

The validation of the intermediates and target compounds (**T1–T18**) involved a combination of analytical techniques, including ^{1}H NMR, ^{13}C NMR, and mass spectrometry. The ^{1}H NMR spectrum of compound **T4** showed two singlet peaks at δ: 12.98 and 10.57 ppm, corresponding to the –NH proton of 1,2,4-triazole and the –OH proton, respectively. The pyrazine ring's three aromatic protons were observed with two singlet peaks at δ: 9.30 and 8.84 ppm and one doublet peak at δ: 8.85 ppm. Additionally, two doublet peaks at δ: 7.95 and 6.90 ppm indicated the presence of four aromatic protons from the phenyl ring. Finally, a sharp singlet peak at δ: 5.13 ppm was attributed to the –CH$_2$ protons. The ^{13}C NMR spectrum of compound **T4** showed characteristic peaks corres-

ponding to its molecular structure. The peaks at δ: 190.28 and 165.39 ppm were assigned to the carbonyl carbon and the carbon attached to the hydroxy group respectively. The two carbons of the 1,2,4-triazole were denoted by peaks at δ 162.90 and 162.87 ppm. The four carbons of the pyrazine ring were represented by peaks at δ: 146.95, 145.02, 143.43, and 138.69 ppm. Five carbons from the phenyl ring were identified by three peaks at δ: 131.21, 126.43, and 115.48 ppm. Furthermore, a peak at δ: 38.88 ppm confirmed the presence of –CH$_2$ carbon. The molecular mass of compound **T4** was unambiguously confirmed through the mass spectrum, revealing a molecular ion peak (M + H peak) observed at (m/z) 314.06. Similarly, the ^{1}H NMR spectrum of compound **T11** presented a singlet peak at δ: 12.97 ppm, signifying the –NH proton of the 1,2,4-triazole. The three aromatic protons within the pyrazine ring manifested as two doublet peaks at δ: 9.39 and 8.81 ppm, along with one triplet peak at δ: 8.77 ppm. In the region of δ: 7.73–7.67 ppm four aromatic protons originating from the phenyl ring were detected. Additionally, a distinct sharp singlet peak at δ: 4.76 ppm represents the presence of –CH$_2$ protons. In the ^{13}C NMR spectrum of compound **T11**, characteristic peaks aligned with its molecular structure. Peaks at δ: 168.19 and 162.49 ppm were assigned to two carbons of 1,2,4-triazole. The four carbons of the pyrazine ring were represented by peaks at δ: 160.02, 145.89, 144.90, and 144.36 ppm. Furthermore, the phenyl ring contributed five peaks in the range of δ: 142.46 to 130.11 ppm, reflecting the presence of six carbon atoms. Peaks at δ: 115.63 and 36.59 ppm were attributed to the –CF$_3$ and –CH$_2$ carbons, respectively. The molecular mass of compound **T11** was conclusively confirmed through mass spectrometry, revealing the presence of the molecular ion peak (M + H peak) at (m/z) 338.18, thus validating its molecular weight.

Computational studies

Pharmacokinetic and physicochemical studies. The comprehensive summary of the pharmacokinetic and physico-

Table 1 Structural details of the target compounds (**T1–T18**)

Compound code	R	Compound code	R
T1, T10	*⟨phenyl⟩	**T7, T12**	*⟨phenyl⟩–F
T2	*⟨phenyl⟩–CH$_3$	**T8, T17**	*⟨phenyl⟩–Cl
T3	*⟨phenyl⟩–O–CH$_3$	**T9, T15**	*⟨phenyl⟩–Br
T4	*⟨phenyl⟩–OH	**T11**	*⟨phenyl⟩–CF$_3$
T5, T18	*⟨phenyl⟩–NO$_2$	**T13**	*⟨phenyl⟩–F
T6, T14	*⟨phenyl⟩–CN	**T16**	*⟨phenyl⟩–Br

The symbol '*' denotes the point of attachment.

chemical characteristics of the target molecules is outlined in Table 2, outlining their potential as promising candidates for advancing drug development. Adhering closely to Lipinski's rule of five, a well-established standard for assessing a compound's suitability for oral administration ensures that all target compounds possess favorable pharmaceutical attributes. Compounds that violate more than one of these criteria often face challenges related to permeability or solubility and are considered less suitable for pharmaceutical advancement. In the scope of this study, all the target compounds adhere to Lipinski's rule of five, thereby confirming their suitability for oral delivery. The evaluation of a drug's safety profile heavily relies on the parameters associated with absorption, distribution, metabolism, and excretion (ADME). All of the target compounds exhibit favorable ADME characteristics. When examining the polar surface area (PSA), a crucial factor in how well a drug is absorbed, we found that the values comfortably fall within the optimal range (ranging from 60.70 to 131.85 Å). Moreover, the favorable values for Caco-2 cell permeability (QPPCaco) and the aqueous solubility parameter (QP log S) (ranging from 54.31 to 1128.37 nm s^{-1} and -5.25 to -3.38, respectively) further enhance the potential for efficient absorption in the intestines. Significantly, the blood–brain partition coefficient (QP log BB) values are within an acceptable range (-2.02 to -0.24), indicating that these compounds can cross the blood–brain barrier. Furthermore, the human serum albumin binding coefficient (QP log Khsa) falls comfortably within the desired range (ranging from -0.50 to 0.20), underscoring the potential of these compounds to effectively bind to human serum albumin, a critical factor in how drugs are distributed in the body. Notably, a majority of these compounds

demonstrate a human oral absorption rate exceeding 85%, which is a strong indicator of their outstanding oral bio-availability. In summary, the comprehensive *in silico* ADME predictions provide strong support for advancing these compounds as promising candidates for further development in drug discovery.

***In silico* molecular docking studies.** *In silico* molecular docking was performed to uncover the binding interactions between a group of target compounds (**T1–T18**) and the receptor, decaprenylphosphoryl-D-ribose oxidase (DprE1) of *Mycobacterium tuberculosis* (PDB ID: 4P8N). DprE1, a vital enzyme in the synthesis of the *M. tuberculosis* cell wall.[29] The computational tool Auto Dock-Vina 1.1.2 was utilized for this purpose. To validate the docking methodology, the ligands from the crystallographic structures of the protein–ligand complexes were reconstructed and then subjected to redocking. The crucial amino acid residues situated in the active site of DprE1, including Arg 58, Ser 59, Ala 64, Ala 72, Gly 76, Gly 125, His 132, Gly 136, Thr 141, Ala 147, Cys 148, Ile 203, Cys387, Tyr 434, and Tyr 415, play a significant role. Most of the target compounds demonstrated interactions with these amino acid residues and exhibited higher binding energy values compared to the reference drugs (PZA, INN, and STM). Compound **T11** docked within the active site of DprE1 with a binding energy of -10.10 kcal mol^{-1} and formed five hydrogen bond interactions with Arg 58, Ser 59, Gly 125, His 132, and Tyr 415 amino acid residues. It also showed a π–σ interaction with Ala 64 and Ile 131 and a π–*alkyl* interaction with Cys 129 and Ala 417 (Fig. 1 and 2). Table 3 provides a comprehensive summary of the binding energies and the amino acid residues engaged by both the target compounds and reference compounds.

Table 2 Pharmacokinetic and physicochemical parameters of the target compounds (**T1–T18**)

Comp.	MW ($\leq$500 Da)	HBD ($\leq$5)	HBA ($\leq$10)	QP log P (o/w) ($\leq$5)	QP log S ($\leq$0.5)	nRB (0–15)	PSA ($\leq$140 Å)	QPPCaco (<25 nm s^{-1} is low; >500 nm s^{-1} is high)	QP log Khsa (-1.5 to 1.5)	QP log BB (-3.0 to 1.2)	%OA (>80% is high; <25% is low)
T1	297.33	1	6.5	1.84	-3.49	4	87.14	454.69	-0.32	-0.95	85.31
T2	311.36	1	6.5	2.10	-4.03	4	87.16	454.22	-0.17	-0.99	86.83
T3	327.36	1	7.25	1.95	-3.73	5	95.37	453.58	-0.32	-1.05	85.90
T4	313.33	2	7.25	1.21	-3.38	5	109.73	137.55	-0.40	-1.57	72.31
T5	342.33	1	7.5	1.13	-3.60	5	131.86	54.32	-0.39	-2.03	64.61
T6	322.34	1	8	1.08	-4.41	5	112.94	96.13	-0.51	-1.78	68.78
T7	315.32	1	6.5	2.02	-3.78	4	87.15	454.64	-0.28	-0.85	86.31
T8	331.78	1	6.5	2.35	-4.23	4	87.14	454.89	-0.22	-0.81	88.27
T9	376.23	1	6.5	2.42	-4.33	4	87.14	454.87	-0.20	-0.80	88.70
T10	269.32	1	4.5	2.61	-3.85	3	60.78	1109.17	-0.05	-0.48	96.73
T11	337.32	1	4.5	3.58	-5.26	3	60.78	1109.04	0.20	-0.24	100
T12	287.31	1	4.5	2.83	-4.19	3	60.78	1109.26	-0.01	-0.38	100
T13	287.31	1	4.5	2.78	-4.08	3	60.77	1109.81	-0.02	-0.40	100
T14	294.33	1	6	1.83	-4.78	4	86.58	234.64	-0.22	-1.29	80.10
T15	348.22	1	4.5	3.17	-4.68	3	60.78	1109.31	0.09	-0.32	100
T16	348.22	1	4.5	3.08	-4.48	3	60.70	1128.37	0.06	-0.33	100
T17	303.77	1	4.5	3.09	-4.57	3	60.78	1109.50	0.06	-0.33	100
T18	314.32	1	5.5	1.88	-3.99	4	105.46	132.99	-0.10	-1.54	75.99

Comp.: compound, MW: molecular weight, HBD: number of hydrogen bond donors, HBA: number of hydrogen bond acceptors, QP log P (o/w): logarithm of the partition coefficient between *n*-octanol and water, QP log S: aqua solubility parameter, nRB: number of rotatable bonds, PSA: polar surface area, QPPCaco: caco-2 cell permeability, QP log Khsa: human serum albumin binding co-efficient, QP log BB: blood/brain partition co-efficient, and %OA: percentage of oral absorption.
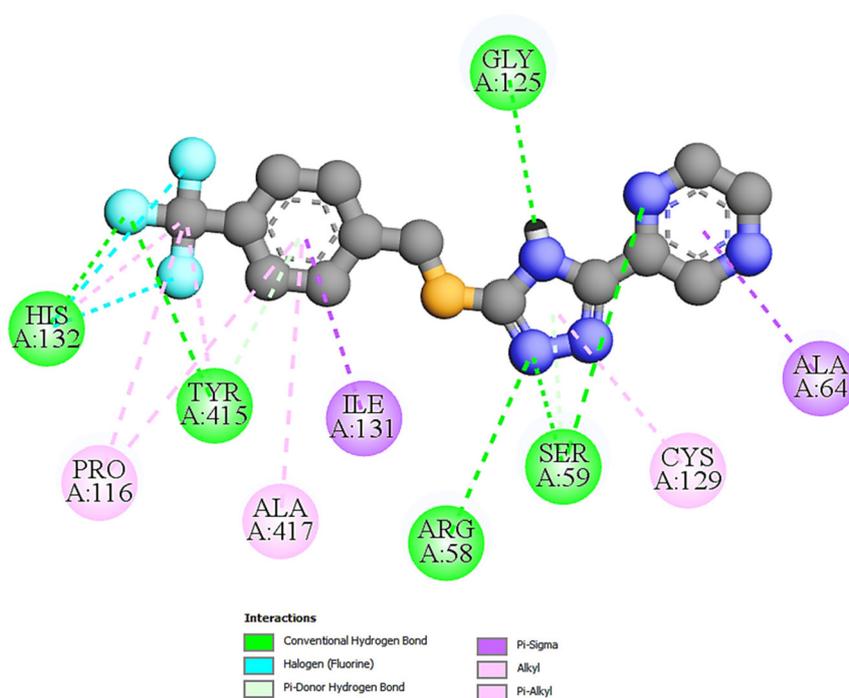
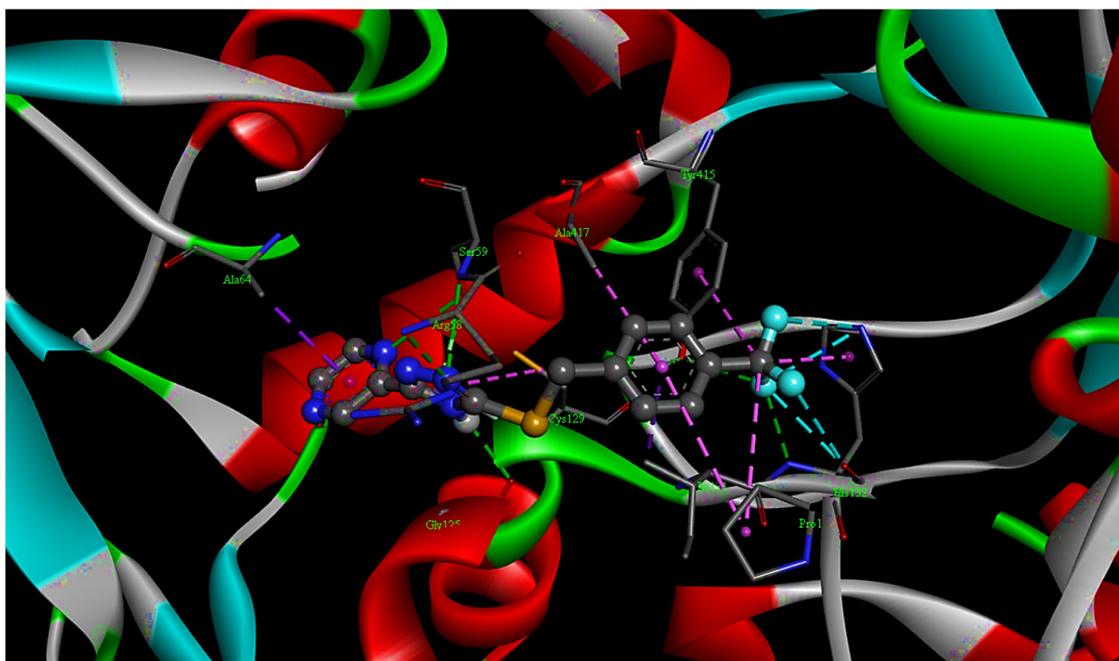**Fig. 1** The 2D docking poses of compound **T11** with receptor 4P8N.

Fig. 2 The 3D docking poses of compound **T11** with receptor 4P8N.

DFT studies. The target molecular entities (**T1–T18**) were subjected to geometric optimization employing density functional theory (DFT) with the B3LYP functional and the 6-31G++ (d, p) basis set. It is imperative to scrutinize the highest occupied molecular orbital and the lowest unoccupied molecular orbital, collectively denoted as the frontier molecular orbitals (FMOs). The HOMO signifies an electron-abundant orbital, whereas the LUMO denotes an electron-deficient one. These FMOs assume a pivotal role in dictating a molecule's interactions with its target counterparts. Generally, a molecule's

Table 3 Binding energy and interactions of target compounds (T1–T18) with receptor 4P8N

Comp.	Binding energy (kcal mol^{-1})	Inhibition constant (K_i) (nM)	No. of H-bonds	Interacting amino acid residues
T1	−8.3	393.27	03	GLY57, ARG58, SER59, CYS129
T2	−9.4	125.14	04	GLY55, GLY57, ARG58, SER59, CYS129
T3	−9.1	156.21	02	ARG58, SER59, TYR60, ALA64
T4	−9.4	125.38	03	ALA53, ARG58, SER59, GLY125
T5	−8.8	277.76	04	SER59, GLY117, THR118, LYS134, GLN336
T6	−9.7	79.26	04	ARG58, SER59, CYS129, ASN63
T7	−9.3	149.61	03	ARG58, SER59, CYS129, ASN63
T8	−8.8	277.93	02	ALA53, SER59, GLY124, GLY125
T9	−8.9	281.47	02	ALA53, SER59, GLY124, GLY125, VAL121
T10	−9.0	243.35	02	SER59, ALA64, VAL121, GLY125, CYS129
T11	−10.1	39.47	05	ARG58, SER59, GLY125, HIS132, TYR415
T12	−9.2	151.87	02	SER59, ALA64, GLY125, CYS129
T13	−9.3	149.82	02	SER59, ALA64, GLY125, CYS129
T14	−9.7	74.65	04	SER59, ALA64, GLY117, GLY125, CYS129
T15	−9.3	149.47	05	SER59, GLY117, THR118, LYS134, TYR415
T16	−9.1	156.07	02	SER59, ALA64, GLY125, CYS129, LYS418
T17	−9.1	156.03	02	SER59, ALA64, GLY125, CYS129
T18	−9.8	69.08	04	ARG58, SER59, ALA64, HIS132, TYR415
PZA	−5.3	21.74 μM	04	GLY57, ARG58, SER59, GLY125, CYS129
INN	−8.2	17.93 μM	04	ALA53, ARG54, THR122, GLY125, ILE184
STM	−9.1	201.09	06	GLY117, HIS132, SER228, GLN336, TYR415

Comp.: compound, PZA: pyrazinamide, INN: ciprofloxacin, STM: streptomycin.

propensity to engage in binding interactions with other molecules tends to diminish as its HOMO energy decreases and its LUMO energy escalates. Table 4 presents the HOMO and LUMO energy values for the target molecules (T1–T18), gleaned from meticulous DFT calculations. Fig. 3a elucidates the visual depictions of the FMOs for the potent molecule T11. The studies conducted *via* DFT discern that within compound T11, the electron cloud of the HOMO predominantly localizes itself across the 1,2,4-triazole ring and the concomitant sulfur atom. Conversely, the LUMO expansively disseminates its elec-

tron cloud across the pyrazine ring. The dimension of the energy differential between the HOMO and the LUMO emerges as a pivotal metric for gauging the compound's reactivity, hardness, and softness. A diminutive energy gap connotes heightened chemical reactivity and an augmented proclivity for intermolecular interactions, thereby categorizing the molecule as intrinsically soft. Conversely, molecules featuring a substantial energy gap exhibit heightened thermal stability and a diminished propensity for intermolecular interactions, thereby classifying them as intrinsically rigid entities.

Table 4 Global reactivity parameters calculated using DFT

Comp.	E_{HOMO} (eV)	E_{LUMO} (eV)	ΔE (eV)	IP (eV)	EA (eV)	η (eV)	σ (eV)	μ (eV)	ω (eV)	χ (eV)
T1	−6.0954	−1.8858	4.2096	6.0954	1.8858	2.1048	0.2376	−2.1048	1.0524	3.9906
T2	−6.0437	−1.8531	4.1906	6.0437	1.8531	2.0953	0.2386	−2.0953	1.0476	3.9484
T3	−6.0518	−1.7905	4.2613	6.0518	1.7905	2.1307	0.2347	−2.1307	1.0653	3.9212
T4	−6.0300	−1.8449	4.1851	6.0300	1.8449	2.0926	0.2389	−2.0926	1.0463	3.9375
T5	−6.3212	−3.1266	3.1946	6.3212	3.1266	1.5973	0.3130	−1.5973	0.7987	4.7239
T6	−6.3049	−2.6694	3.6354	6.3049	2.6694	1.8177	0.2751	−1.8177	0.9089	4.4872
T7	−6.1362	−1.9184	4.2178	6.1362	1.9184	2.1089	0.2371	−2.1089	1.0544	4.0273
T8	−6.1743	−2.0871	4.0872	6.1743	2.0871	2.0436	0.2447	−2.0436	1.0218	4.1307
T9	−6.1824	−2.1034	4.0790	6.1824	2.1034	2.0395	0.2452	−2.0395	1.0197	4.1429
T10	−6.0437	−1.8585	4.1851	6.0437	1.8585	2.0926	0.2389	−2.0926	1.0463	3.9511
T11	−6.2178	−1.9619	4.2559	6.2178	1.9619	2.1279	0.2350	−2.1279	1.0640	4.0899
T12	−6.1144	−1.8994	4.2150	6.1144	1.8994	2.1075	0.2372	−2.1075	1.0538	4.0069
T13	−6.0573	−1.8558	4.2014	6.0573	1.8558	2.1007	0.2380	−2.1007	1.0504	3.9565
T14	−6.3130	−2.0218	4.2912	6.3130	2.0218	2.1456	0.2330	−2.1456	1.0728	4.1674
T15	−6.1688	−1.9347	4.2341	6.1688	1.9347	2.1170	0.2362	−2.1170	1.0585	4.0518
T16	−6.0709	−1.8613	4.2096	6.0709	1.8613	2.1048	0.2376	−2.1048	1.0524	3.9661
T17	−6.1661	−1.9293	4.2368	6.1661	1.9293	2.1184	0.2360	−2.1184	1.0592	4.0477
T18	−6.3457	−2.6096	3.7361	6.3457	2.6096	1.8681	0.2677	−1.8681	0.9340	4.4776
PZA	−6.7838	−1.9347	4.8491	6.7838	1.9347	2.4246	0.2062	−2.4246	1.2123	4.3592
INN	−5.7007	−1.2027	4.4980	5.7007	1.2027	2.2490	0.2223	−2.2490	1.1245	3.4517

Comp.: compound, bandgap (ΔE) = E_{HOMO} − E_{LUMO}, ionization potential (IP) = −E_{HOMO}, electron affinity (EA) = −E_{LUMO}, chemical hardness (η) = (IA − EA)/2, chemical softness (σ) = 1/2η, chemical potential (μ) = −η, electrophilicity index (ω) = η/2, and electronegativity (χ) = (IP + EA)/2.
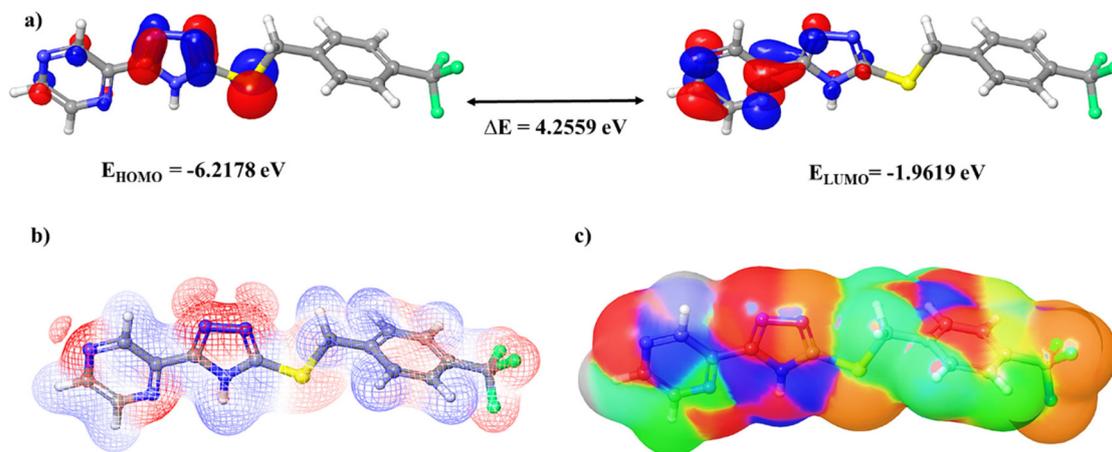
Fig. 3 (a) Frontier molecular orbitals, (b) molecular electrostatic potentials, and (c) the electron density surface of compound **T11**.

Comprehending overarching chemical reactivity descriptors on a global scale is imperative for establishing intricate correlations among the structural attributes, stability, and reactivity of a molecule.[30] These descriptors are ascertained through the meticulous evaluation of the HOMO and LUMO energy levels of the molecules, with precise numerical values delineated in Table 4.[31] An elevated chemical softness parameter signifies an augmented proclivity for binding with the receptor, whereas an increased chemical hardness value implies a diminished inclination for binding. Significantly, all scrutinized compounds manifest heightened chemical softness and diminished chemical hardness in contrast to the reference pharmaceutical agents. With the augmentation of the chemical potential, the discernibility of interaction between the ligand and the receptor intensifies, and notably, all target compounds manifest elevated chemical potential values in comparison to the benchmark pharmaceuticals. The electrophilicity index and electronegativity serve as metrics gauging a molecule's capacity to attract electrons from its ambient milieu. Molecules endowed with a heightened electrophilicity index and electronegativity values evince an augmented predisposition for forging interactions with receptors. It is of significance that all target compounds exhibit electronegativity and electrophilicity index values akin to those inherent in the reference pharmaceuticals. Fig. 3c elucidates the electron density surface of compound **T11**. The ionization potential (IP) and electron affinity (EA) serve as quantitative measures for appraising a molecule's proclivity to either gain or relinquish electrons within its proximate milieu. In the general context, diminished values of IP and EA are correlated with an increased proclivity toward toxicity. It merits emphasis that all investigated compounds align within the stipulated IP and EA value range characteristic of the FDA-approved pharmaceuticals, with EA values spanning the range from −3 to 7 eV and IP values encompassing the interval of 4–15 eV.

To evaluate the reactivity of these compounds, we undertook molecular electrostatic potential (MEP) computations, a pivotal methodology for prognosticating the interaction modalities of these target compounds based on their physicochemical attributes and comprehending their predisposition toward electrophilic and nucleophilic reactions.[32] Through the employment of DFT, we ascertained the MEP profiles of the specified compounds. In Fig. 3b, the MEPs of compound **T11** are delineated in detail, with the MEP surface meticulously color-coded for optimal elucidation. The blue domains in the figure delineate regions characterized by a positive electrostatic potential, while the red domains signify areas distinguished by a negative electrostatic potential. The white regions denote a neutral electrostatic potential. Across the entirety of these molecules, regions characterized by a negative electrostatic potential are chiefly congregated in the proximity of nitrogen, sulfur, and fluorine atoms. Conversely, zones exhibiting a positive electrostatic potential are predominantly situated in the vicinity of hydrogen atoms and an intricately structured phenyl ring.

Biological studies

Antitubercular activity. The MABA technique was employed to assess the efficacy of target compounds (**T1**–**T18**) against *Mycobacterium tuberculosis* H37Rv (ATCC27294). The results presented in Table 5 indicate that the minimum inhibitory concentration (MIC) values range from 9.25 to 46.45 μM (3.12 to 12.5 μg mL^{-1}). Notably, compound **T11** exhibited the highest potency among the tested compounds, displaying a MIC of 9.25 μM (3.12 μg mL^{-1}), which is comparable to the effectiveness of INN and STM, and surpasses PZA by a factor of two. Furthermore, compounds **T4**, **T5**, **T6**, **T14**, **T15**, **T16**, and **T18** demonstrated promising antitubercular activity with MIC values ranging from 18.01 to 21.25 μM (6.25 μg mL^{-1}). While not as potent as STM and INN, they exhibited effectiveness comparable to that of PZA. The remaining compounds exhibited moderate antitubercular activity, with MIC values ranging from 33.33 to 46.45 μM (12.5 μg mL^{-1}). These experimental findings closely align with predictions from computer-based simulations. Docking analyses suggest that the most potent compounds possess the strongest binding energies.

Table 5 Antitubercular activity of compounds **T1–T18** with *M. tuberculosis* H37Rv

	M. tuberculosis H37Rv			*M. tuberculosis* H37Rv	
Comp.	MIC (μg mL^{-1})	MIC (μM)	Comp.	MIC (μg mL^{-1})	MIC (μM)
T1	12.5	42.07	**T12**	12.5	43.54
T2	12.5	40.18	**T13**	12.5	43.54
T3	12.5	38.21	**T14**	6.25	21.25
T4	6.25	19.96	**T15**	6.25	18.01
T5	6.25	18.27	**T16**	6.25	18.01
T6	6.25	19.40	**T17**	12.5	41.25
T7	12.5	39.67	**T18**	6.25	19.90
T8	12.5	37.76	**PZA**	3.12	25.34
T9	12.5	33.33	**STM**	6.25	10.74
T10	12.5	46.45	**INN**	3.12	9.41
T11	3.12	9.25			

Comp.: compound, PZA: pyrazinamide, STM: streptomycin, INN: ciprofloxacin.

Table 6 Antibacterial activity (MIC in mg mL^{-1}) of the target compounds (**T1–T18**)

	MIC (mg mL^{-1})			
Comp.	*S. aureus*	*S. mutans*	*E. coli*	*S. typhi*
T1	2.5	>5.0	5.0	>5.0
T2	2.5	>5.0	5.0	>5.0
T3	5.0	5.0	5.0	>5.0
T4	2.5	1.25	0.625	>5.0
T5	1.25	>5.0	>5.0	>5.0
T6	5.0	>5.0	>5.0	>5.0
T7	2.5	>5.0	5.0	>5.0
T8	5.0	5.0	5.0	>5.0
T9	0.01953	1.25	>5.0	1.25
T10	0.625	2.5	5.0	>5.0
T11	5.0	5.0	1.26	5.0
T12	2.5	5.0	5.0	5.0
T13	2.5	5.0	5.0	5.0
T14	2.5	>5.0	>5.0	>5.0
T15	2.5	5.0	2.5	>5.0
T16	0.01953	0.01953	0.625	2.5
T17	2.5	>5.0	>5.0	5.0
T18	0.625	>5.0	1.25	5.0
STM	0.012	0.010	0.010	0.011
CHL	0.010	0.010	0.012	0.010
Control	00	00	00	00

Comp.: compound, STM: streptomycin, CHL: chloramphenicol, control: DMSO.

Table 7 Antifungal activity (MIC in mg mL^{-1}) of the target compounds (**T1–T18**)

	MIC (mg mL^{-1})		MIC (mg mL^{-1})
Comp.	*A. niger*	Comp.	*A. niger*
T1	2.5	**T11**	1.25
T2	5.0	**T12**	0.625
T3	5.0	**T13**	5.0
T4	5.0	**T14**	0.625
T5	5.0	**T15**	1.25
T6	5.0	**T16**	2.5
T7	5.0	**T17**	5.0
T8	2.5	**T18**	5.0
T9	5.0	AmB	0.004
T10	5.0	Control	00

Comp.: compound, AmB: amphotericin B, control: DMSO.

Additionally, density functional theory analyses indicate that the most effective compounds exhibit higher values for properties such as chemical softness, chemical potential, electrophilicity, and electronegativity.

Antibacterial activity. The *in vitro* antibacterial activity of the target compounds (**T1–T18**) was tested using the broth microdilution method and the MIC values were measured in mg mL^{-1}. All the synthesized compounds were screened against two Gram-positive bacterial strains (*S. aureus* and *S. mutans*), and two Gram-negative bacterial strains (*E. coli* and *S. typhi*) using streptomycin (STM) and chloramphenicol (CHL) as the standard drugs. The MIC values of the target compounds along with those of standard drugs for comparison are presented in Table 6. Among the screened compounds, **T9**, **T10**, **T16**, and **T18** demonstrated significant inhibition activity against *S. aureus*, whereas compound **T16** was active against *S. mutans*. Compounds **T4**, and **T16** were potent against both *E. coli*. None of the compounds showed notable inhibition activity against *S. typhi*.

Antifungal activity. The *in vitro* antifungal activity of the title compounds (**T1–T18**) was screened using the broth microdilution method and the MIC values were measured in mg mL^{-1}. All the synthesized compounds were screened against the fungal strain *A. niger* using amphotericin B (AmB) as a standard drug. The MIC values of the target compounds along with the standard drugs for comparison are presented in Table 7. Among the screened compounds **T12** and **T14** showed significant inhibition activity against *A. niger*. Compounds **T11** and **T15** demonstrated moderate inhibition activity against the tested strain.

Cytotoxicity studies. The MTT assay served as the modality for the assessment of cytotoxicity of compounds exhibiting a MIC of 21.25 μM or lower in the context of antituberculosis screening. Table 8 shows the inhibitory impact these efficacious compounds exerted on the proliferation of Vero cells (African green monkey kidney cell line, Catalog number 11965-

092) at concentrations spanning 25, 50, 75, and 100 μM. Notably, it was observed that all the tested potent compounds did not exhibit significant toxicity, as indicated by IC$_{50}$ values exceeding 375 μM, as shown in Table 9. Additionally, it is important to highlight that none of these compounds had adverse effects on normal cells, indicating the absence of general cellular toxicity.

Structure–activity relationship. The effectiveness of the target compounds (**T1–T18**) in terms of their anti-tubercular and antimicrobial properties reveals specific structure–activity relationships (SAR). The introduction of substituents that enhance the aromaticity and electron density within the pyrazine or 1,2,4-triazole ring resulted in improved antitubercular activity. Both 1-phenyl-2-((5-(pyrazin-2-yl)-4*H*-1,2,4-triazol-3-yl)

Table 8 Cell growth inhibition of active compounds against Vero cells

Compound	% of inhibition			
	25 μM	50 μM	75 μM	100 μM
T4	3.21 ± 0.34	6.46 ± 0.21	9.61 ± 0.18	12.92 ± 0.26
T5	3.05 ± 0.23	6.38 ± 0.17	9.53 ± 0.15	12.87 ± 0.19
T6	3.14 ± 0.27	6.35 ± 0.32	9.89 ± 0.23	13.05 ± 0.23
T11	2.97 ± 0.15	6.03 ± 0.22	9.08 ± 0.27	12.10 ± 0.14
T14	3.02 ± 0.18	6.24 ± 0.31	9.63 ± 0.20	13.09 ± 0.17
T15	2.99 ± 0.31	6.12 ± 0.19	9.74 ± 0.38	12.64 ± 0.27
T16	3.04 ± 0.25	6.16 ± 0.27	9.37 ± 0.16	12.35 ± 0.22
T18	3.17 ± 0.23	6.38 ± 0.22	9.71 ± 0.21	12.59 ± 0.25

The values represent the mean ± standard error of the mean obtained from three separate determinations after 72 hours of exposure.

Table 9 IC_{50} values of active compounds obtained through an MTT assay against Vero cells

Compound	IC_{50} (μM)	Compound	IC_{50} (μM)
T4	387.53 ± 10.15	**T14**	379.86 ± 11.47
T5	387.29 ± 12.03	**T15**	389.47 ± 10.73
T6	379.88 ± 10.49	**T16**	402.72 ± 13.48
T11	412.32 ± 11.63	**T18**	393.80 ± 12.44

The IC_{50} values represent the concentration of a substance required to inhibit 50% of cell viability calculated after a 72-hour exposure.

thio)ethan-1-one (**T1–T9**) and 2-(5-(benzylthio)-4*H*-1,2,4-triazol-3-yl)pyrazine derivatives (**T10–T18**) exhibited superior activity when equipped with electron-withdrawing groups. For instance, **T5** and **T18** with a nitro group as well as **T6** and **T14** with a cyano group are equipotent (MIC of 6.25 μg mL^{-1}). The introduction of a –CF$_3$ (trifluoromethyl) group (**T11**) into the active pharmacophore further improved the antimycobacterial activity (MIC of 3.12 μg mL^{-1}). This improvement is attributed to the small size of fluorine, which closely resembles hydrogen and can meet the steric requirements for interaction with the receptor enzyme. Additionally, it enhances lipid solubility, thereby improving the absorption rate. Fluorinated analogues also offer increased thermal and oxidative stability to the compounds, as the carbon–fluorine (C–F) bond exhibits greater bond strength relative to the carbon–hydrogen (C–H) bond. Furthermore, the fluorine substituent can form hydrogen bonds with target enzymes. The substitution of the –CF$_3$ group is more favorable than the –F group, as it is more lipophilic. Hence it can be concluded that compound **T11** exhibited the highest potency among the tested compounds primarily due to the presence of the –CF$_3$ substituent.

Conclusions

This study entailed the synthesis of a new series of 1-phenyl-2-((5-(pyrazin-2-yl)-4*H*-1,2,4-triazol-3-yl)thio)ethan-1-one (**T1–T9**) and 2-(5-(benzylthio)-4*H*-1,2,4-triazol-3-yl)pyrazine (**T10–T18**) derivatives. The synthesized compounds were characterized using various analytical techniques. The compounds under-

went *in vitro* testing to assess their potential as antimicrobial agents against diverse bacteria, fungi, and the tuberculosis-inducing *M. tuberculosis* H37Rv strain. Among the tested compounds, eight exhibited notable activity against tuberculosis, with a MIC ≤ 6.25 μg mL^{-1}. Particularly noteworthy was compound **T11**, showcasing the most potent activity with a MIC of 3.12 μg mL^{-1}. To ascertain their suitability for pharmaceutical development, cytotoxicity evaluations were conducted, revealing that these active compounds did not induce harm to normal cells. Additionally, computational analysis was employed to scrutinize the binding interactions between these compounds and the active site of the DprE1 enzyme through *in silico* molecular docking. Although these studies indicated strong binding interactions, further experimental validation is necessary to confirm the mechanism of inhibition action. DFT studies provided insights into the electronic properties of these compounds, indicating a narrower HOMO–LUMO energy gap, augmented chemical softness, diminished chemical hardness, lower electron affinity, and higher chemical potential in comparison with reference compounds. These findings collectively imply heightened reactivity and more robust interactions with the target receptor. Beyond their antitubercular attributes, compounds **T9**, **T10**, and **T18** manifested significant antibacterial activity against *S. aureus*, whereas compound **T16** exhibited antibacterial activity against *S. aureus*, *S. mutans*, and *E. coli*. Compounds **T12** and **T14** evinced substantial antifungal activity against *A. niger*. This exhaustive study emphasizes the importance of further delving into the pharmacological characteristics of these compounds, inclusive of *in vivo* investigations, to comprehensively fathom their potential in combating infectious diseases.

Author contributions

Shivakumar: conceptualization, methodology, computational studies, data curation, visualization, biological studies, and writing – original draft. P Dinesha: data curation and visualization. Vanishree A. L.: data curation and visualization. Udayakumar D.: supervision, validation, and writing – review and editing. Varsha Prakash Shetty: bacterial and fungal activity. Vijaya Kumar Deekshit: bacterial and fungal activity.

Conflicts of interest

The authors declare that they have no known competing financial interests or personal relationships that could have appeared to influence the work reported in this paper.

Acknowledgements

References

1 Global tuberculosis report 2023, World Health Organization, 2023, ISBN 978-92-4-008385-1.

2 A. Gupta, S. Juneja, S. Sahu, M. Yassin, G. Brigden, E. Wandwalo, S. Rane, F. Mirzayev and M. Zignol, *PLOS Glob. Public Health*, 2022, **2**, e0001287, DOI: 10.1371/journal.pgph.0001287.

3 V. Singh and K. Chibale, *Acc. Chem. Res.*, 2021, **54**, 2361–2376, DOI: 10.1021/acs.accounts.0c00878.

4 G. Stelitano, J. C. Sammartino and L. R. Chiarelli, *Molecules*, 2020, **25**, 1239, DOI: 10.3390/molecules25051239.

5 P. Miniyar, P. Murumkar, P. Patil, M. Barmade and K. Bothara, *Mini-Rev. Med. Chem.*, 2013, **13**, 1607–1625, DOI: 10.2174/1389557511313110007.

6 V. Rangaswamy and U. Laddi, *Antiinfect. Agents*, 2023, **21**, e111023222113, DOI: 10.2174/0122113525268198230921071016.

7 Y. Zhang, W. Shi, W. Zhang and D. Mitchison, *Microbiol. Spectr.*, 2014, **2**, DOI: 10.1128/microbiolspec.mgm2-0023-2013.

8 R. Reddyrajula and U. Dalimba, *Bioorg. Med. Chem. Lett.*, 2020, **30**, 126846, DOI: 10.1016/j.bmcl.2019.126846.

9 S. Srinivasarao, A. Nandikolla, A. Suresh, K. Van Calster, L. De Voogt, D. Cappoen, B. Ghosh, H. Aggarwal, S. Murugesan and K. V. G. Chandra Sekhar, *RSC Adv.*, 2020, **10**, 12272–12288, DOI: 10.1039/d0ra01348j.

10 M. Panda, S. Ramachandran, V. Ramachandran, P. S. Shirude, V. Humnabadkar, K. Nagalapur, S. Sharma, P. Kaur, S. Guptha, A. Narayan, J. Mahadevaswamy, A. Ambady, N. Hegde, S. S. Rudrapatna, V. P. Hosagrahara, V. K. Sambandamurthy and A. Raichurkar, *J. Med. Chem.*, 2014, **57**, 4761–4771, DOI: 10.1021/jm5002937.

11 S. Zhou, S. Yang and G. Huang, *J. Enzyme Inhib. Med. Chem.*, 2017, **32**, 1183–1186, DOI: 10.1080/14756366.2017.1367774.

12 S. Kumar, P. Dinesha, D. Udayakumar, V. P. Shetty and V. K. Deekshit, *J. Mol. Struct.*, 2024, **1304**, 137657, DOI: 10.1016/j.molstruc.2024.137657.

13 Z. Karczmarzyk, M. Swatko-Ossor, W. Wysocki, M. Drozd, G. Ginalska, A. Pachuta-Stec and M. Pitucha, *Molecules*, 2020, **25**, 6033, DOI: 10.3390/MOLECULES25246033.

14 T. Oh, A. Hayat, E. Yoo, S. N. Cho, Y. Y. Sheen, D. K. Kim and H. Y. P. Choo, *Bull. Korean Chem. Soc.*, 2015, **36**, 43–51, DOI: 10.1002/bkcs.10009.

15 G. Karabanovich, J. Dušek, K. Savková, O. Pavliš, I. Pávková, J. Korábečný, T. Kučera, H. Kočová Vlčková, S. Huszár, Z. Konyariková, K. Konečná, O. Jand'Ourek, J. Stolaříková, J. Korduláková, K. Vávrová, P. Pávek, V. Klimešová, A. Hrabálek, K. Mikušová and J. Roh, *J. Med. Chem.*, 2019, **62**, 8115–8139, DOI: 10.1021/acs.jmedchem.9b00912.

16 F. E. Bradford, L. P. Connor, C. A. Kilner and M. A. Halcrow, *Polyhedron*, 2004, **23**, 2141–2151, DOI: 10.1016/j.poly.2004.06.018.

17 S. R. Patil, A. Asrondkar, V. Patil, J. N. Sangshetti, F. A. Kalam Khan, M. G. Damale, R. H. Patil, A. S. Bobade and D. B. Shinde, *Bioorg. Med. Chem. Lett.*, 2017, **27**, 3845–3850, DOI: 10.1016/j.bmcl.2017.06.053.

18 L. R. Zhang, Z. J. Liu, H. Zhang, J. Sun, Y. Luo, T. T. Zhao, H. Bin Gong and H. L. Zhu, *Bioorg. Med. Chem.*, 2012, **20**, 3615–3621, DOI: 10.1016/j.bmc.2012.03.061.

19 J. Vrbanac and R. Slauter, in *A Comprehensive Guide to Toxicology in Nonclinical Drug Development*, Elsevier, 2016, pp. 39–67. DOI: 10.1016/B978-0-12-803620-4.00003-7.

20 H. Beard, A. Cholleti, D. Pearlman, W. Sherman and K. A. Loving, *PLoS One*, 2013, **8**, e82849, DOI: 10.1371/journal.pone.0082849.

21 J. Eberhardt, D. Santos-Martins, A. F. Tillack and S. Forli, *J. Chem. Inf. Model.*, 2021, **61**, 3891–3898, DOI: 10.1021/acs.jcim.1c00203.

22 O. Trott and A. J. Olson, *J. Comput. Chem.*, 2009, **31**, 455–461, DOI: 10.1002/jcc.21334.

23 K. R. Cousins, *J. Am. Chem. Soc.*, 2005, **127**, 4115–4116, DOI: 10.1002/jcc.21334.

24 A. Fiser, R. Kinh, G. Do and A. S. Ali, *Modeling of loops in protein structures*, 2000, https://www.rcsb.org0pdb.

25 J. Yang, A. Roy and Y. Zhang, *Bioinformatics*, 2013, **29**, 2588–2595, DOI: 10.1093/bioinformatics/btt447.

26 J. Tirado-Rives and W. L. Jorgensen, *J. Chem. Theory Comput.*, 2008, **4**, 297–306, DOI: 10.1021/ct700248k.

27 S. G. Franzblau, R. S. Witzig, J. C. Mclaughlin, P. Torres, G. Madico, A. Hernandez, M. T. Degnan, M. B. Cook, V. K. Quenzer, R. M. Ferguson and R. H. Gilman, *J. Clin. Microbiol.*, 1998, **36**, 362–366, DOI: 10.1128/jcm.36.2.362-366.1998.

28 M. R. Espíndola, F. de P. Varotti, A. C. C. Aguiar, S. N. Andrade and E. M. M. da Rocha, *Braz. J. Pharm. Sci.*, 2022, **58**, e18308, DOI: 10.1590/s2175-97902022e18308.

29 J. Gawad and C. Bonde, *Chem. Cent. J.*, 2018, **12**, 72, DOI: 10.1186/s13065-018-0441-2.

30 A. Bendjeddou, T. Abbaz, A. Gouasmia and D. Villemin, *Acta Chim. Pharm. Indica*, 2016, **6**, 32–44.

31 P. S. Sen Gupta, H. R. Bhat, S. Biswal and M. K. Rana, *J. Mol. Liq.*, 2020, **320**, 114375, DOI: 10.1016/j.molliq.2020.114375.

32 M. G. Srinivasa, Shivakumar, D. U. Kumar, C. H. Mehta, U. Y. Nayak and B. C. Revanasiddappa, *J. Comput. Biophys. Chem.*, 2024, **23**, 117–136, DOI: 10.1142/S2737416523500540.